WILEY | Hindawi

Research Article

Enhanced Photovoltaic Properties of Dye-Sensitized Solar Cells through Ammonium Hydroxide-Modified (Nitrogen-Doped) Titania Photoanodes

Tharmakularasa Rajaramanan [ID],[1,2] **Fatemeh Heidari Gourji** [ID],[1]
Dhayalan Velauthapillai [ID],[1] **Punniamoorthy Ravirajan** [ID],[2]
and Meena Senthilnanthanan [ID][3]

[1]*Faculty of Engineering and Science, Western Norway University of Applied Sciences, P.O. Box 7030, 5020 Bergen, Norway*
[2]*Clean Energy Research Laboratory, Department of Physics, University of Jaffna, Jaffna 40000, Sri Lanka*
[3]*Department of Chemistry, University of Jaffna, Jaffna 40000, Sri Lanka*

Correspondence should be addressed to Dhayalan Velauthapillai; dhayalan.velauthapillai@hvl.no
and Meena Senthilnanthanan; meena@univ.jfn.ac.lk

Doping is a unique strategy to modulate the optical and electronic properties of semiconducting materials. This study reports a facile approach to fabricate nitrogen-doped TiO_2 (N-doped TiO_2) photoanode for DSSC application. A solid-state reaction was employed to synthesize a series of N-doped TiO_2 nanoparticles with different volumetric ratios of nitrogen dopant and the TiO_2 host. The NH_4OH as a nitrogen dopant was combined with P25-TiO_2 via grinding followed by calcination at 500°C. The synthesized nanoparticles were extensively characterized by XRD, XPS, EDX, SEM, and TEM techniques. XRD results suggested that the incorporation of nitrogen had not altered the structure of the TiO_2 lattice, and the presence of nitrogen was confirmed through the XPS and EDX spectroscopies. SEM and TEM images, obtained before and after N doping, showed that N-doped TiO_2 nanoparticles with low amounts of NH_4OH (10 and 20 μL) had retained their spherical shapes and sizes while use of higher amounts of the N dopant (30 and 40 μL) had led to agglomeration of nanoparticles. BET and BJH analyses revealed that the optimized N-doped TiO_2 with 20 μL of NH_4OH (20N-TiO_2) possesses the highest average pore diameter of 15.99 nm. Furthermore, the UV-visible spectroscopic analysis confirmed a red shift in the optical absorption edge on N doping and the corresponding bandgap reduced from 3.15 to 2.94 eV with increase in the amount of NH_4OH from 0 to 40 μL. Eventually, DSSCs were fabricated using the prepared pure TiO_2 and N-doped TiO_2 photoanodes, N719 dye, I^-/I_3^- electrolyte, and Pt counter electrode, followed by investigating their performance under simulated irradiation with 100 mW/cm^2 intensity with AM 1.5 filter. The photoanode doped with 20 μL of NH_4OH (20N-TiO_2) exhibited the highest power conversion efficiency (PCE) of about 6.16%, which was 20% higher than that of the control device, with improved J_{SC}. This enhancement in J_{SC} could be predominantly attributed to higher dye uptake along with marginal contribution by reduced rate of recombination. Among the reported studies on DSSCs with N-doped P25-TiO_2 photoanodes, our method gives the best efficiencies for the DSSCs.

1. Introduction

Dye-sensitized solar cells (DSSCs) are being widely studied in the photovoltaic (PV) field for clean and sustainable energy supply. Due to its low-cost fabrication procedure, ecofriendliness, and working ability under low light intensity, it is considered as a more promising technology than other types of photovoltaic devices [1, 2]. Generally, a DSSC is comprised of a dye-sensitized semiconducting metal oxide as photoanode in combination with a redox electrolyte and a

counter electrode [3]. Each component of the DSSC demonstrates its own significance in improving the power conversion efficiency (PCE). However, the photoanode plays a major role in the light harvest and charge transport processes [4]. To date, various semiconducting metal oxides have been studied in DSSCs as photoanode materials [5]. Among them, TiO_2, ZnO, and SnO_2 are widely explored [6]. For example, Wanninayake et al. have reported that SnO_2 performs high election mobility as photoanode. However, the PV performance is considerably low for SnO_2-based devices due to high electron recombination [7]. ZnO, as photoanode in DSSCs, shows several desired features such as relatively high electron mobility in compact form and high exciton binding energy [8–10]. However, ZnO-based devices are unable to compete with the TiO_2-based cells in photovoltaic performance as ZnO possesses lower internal surface area than TiO_2 which reduces its dye anchoring capacity compared to TiO_2 [8, 9]. So far, TiO_2 remains the most promising mesoporous metal oxide employed in DSSCs due to its outstanding properties such as high transparency under visible light, high refractive index, biocompatibility, thermal stability, nontoxicity, and highly porous nature resulting in large surface area for dye anchoring [11, 12]. However, slow charge transport and wide bandgap of the TiO_2 limit further enhancement in PCE of TiO_2-based DSSCs [13]. Doping is largely explored to address the aforementioned limitations of TiO_2-based DSSCs [14].

In general, a dopant modifies both the electronic band structures and surface states of TiO_2 lattice, which in turn affect important properties such as the conduction band energy, charge transport, recombination, and collection [15]. Both metal and nonmetal ions are potential candidates for doping. However, employing a metal ion as dopant may block the anchoring of dye molecules on Ti^{4+} ions due to possible strong coupling between the metal dopant and dye molecules which in turn may reduce dye absorption [15]. The said limitation could be avoided by doping TiO_2 with a nonmetal ion that may result in high dye absorption and efficient electron injection [16]. Moreover, nonmetals can gain more electrons due to their large ionization energies and high electronegativities [17]. Also, nonmetal ions are the only anionic dopants that strongly influence the valance band (VB) of TiO_2. Various nonmetal ions have been investigated as dopants on TiO_2 (N [18], F [19], C [20], S [21], B [22], and I [23]) to improve the PV performance of DSSCs. Among them, nitrogen is considered as the prominent nonmetal candidate. When TiO_2 is doped with N, the hybridization between the 2p orbitals of nitrogen (N) and oxygen (O) results in bandgap narrowing that leads to visible light absorption [24]. Moreover, enhanced photocurrent due to retarded electron recombination has been observed in N-doped TiO_2-based DSSCs [25]. It has also been reported that N doping reduces the oxygen deficiency of TiO_2 and thereby enhances the lifetime of the device [26].

Considering the advantages of N doping, several studies regarding N doping on TiO_2 using different synthetic procedures and its' influence on the performance of DSSCs have been prompted recently. Kang et al. synthesized a N-doped

TiO_2-based photoanode through the sol-gel method, and the corresponding fabricated device showed the maximum PCE of 4.86% compared to the control device (3.73%). This enhancement in PCE was mainly attributed to the increase in the near-visible absorbance due to nitrogen doping and partially to the morphological properties of the N-doped TiO_2 film [18]. In another study carried out by Motlak et al., N-doped TiO_2 nanofibers, prepared by electrospinning and hydrothermal treatment processes, exhibited PCE of 4.7% due to enhanced electron injection, long electron lifetime, and retarded charge recombination [27]. In a separate study, Guo et al. synthesized a hierarchical macro-mesoporous N-doped TiO_2 structure with parallel macrochannels through the template-free wet method which exhibited PCE of 7.27% (device active area $0.16 \, cm^{-2}$) due to the improved dye uptake [28]. Moreover, a few studies have investigated the performance of N-doped TiO_2-based device by varying the nitrogen dopant source [25, 29]. Since N-doped TiO_2 photoelectrode is found to be a promising candidate for PV applications, a facile synthetic route along with a suitable nitrogen source is necessary for its' large-scale synthesis and possible applications.

Among the different methods used for the synthesis of N-doped TiO_2 nanomaterials, doping with commercially available P25-TiO_2 is more time saving and efficient way for large-scale synthesis. Though many sources are available for the synthesis of N-doped TiO_2 by different methods (urea, thiourea, $N_{2(g)}$, $NH_{3(g)}$, etc.), NH_4OH was chosen as the nitrogen source for this study because of its' liquid nature, which enabled easy and uniform mixing of NH_4OH with P25-TiO_2 nanoparticles during the grinding process. Also, this avoids doping of impurities such as C and S with TiO_2 during the doping process. Further, the application of N-doped TiO_2 (utilizing NH_4OH as a nitrogen source) in DSSC fabrication has not been reported previously to the best of our knowledge. Generally, the PV performance of doped TiO_2-based DSSCs depends on the employed nitrogen source, doping method, and TiO_2 properties.

In this regard, we initially prepared N-doped TiO_2 nanoparticles through a solid-state reaction by varying the volumetric ratio between P25-TiO_2 and ammonium hydroxide (NH_4OH). Then, the corresponding films were prepared from the said nanoparticles and sintered at 500°C. Subsequently, the prepared N-doped TiO_2 nanoparticles were characterized structurally and optically followed by investigation on charge transport properties together with PV performance of the fabricated N-doped TiO_2 photoanode-based DSSCs.

2. Materials and Methods

2.1. Materials. All reagents and solvents were purchased from commercial sources: titanium dioxide (TiO_2) nanopowder (21 nm primary particle size, ≥99.5% trace metal basis, Sigma-Aldrich), ammonium hydroxide (NH_4OH) (~25% NH_3 basis, Sigma-Aldrich), Triton TM X-100 (laboratory grade, Sigma-Aldrich), di-tetrabutylammonium *cis*-bis(isothiocyanato)bis(2,2′-bipyridyl-4,4′-dicarboxylato)ruthenium(II) dye (N-719) (95%, Sigma-Aldrich), acetonitrile (CH_3CN) (≥99.9%, Sigma-Aldrich), *tert*-butyl alcohol

+ Anatase (JCPDS card no. 21-1272)
* Rutile (JCPDS card no. 21-1276)
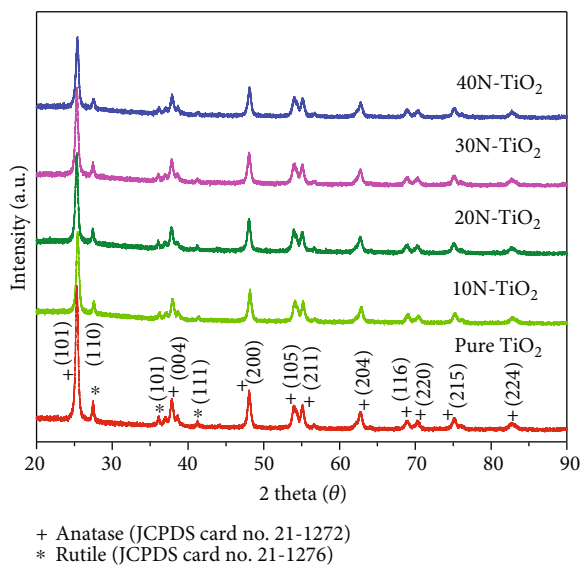
FIGURE 1: XRD patterns of pure TiO_2, 10N-TiO_2, 20N-TiO_2, 30N-TiO_2, and 40N-TiO_2 nanoparticles.

($C_4H_{10}O$) (≥99.7%, Sigma-Aldrich), and acetylacetone ($C_5H_8O_2$) (≥99.5%, Fluka Analytical).

2.2. Preparation of N-Doped TiO_2 Photoanodes and Fabrication of DSSCs.

The fluorine-doped tin oxide- (FTO-) coated conducting glass sheets (sheet resistance 7.5 Ω/cm² and size 2×1 cm²) were cleaned initially with soap water and subsequently with distilled water and ethanol using an ultrasonic bath. The undoped and N-doped (with systematically varied N contents) TiO_2 films were prepared by grinding 100 mg of P25-TiO_2 separately with 0, 10, 20, 30, and 40 μL of NH_4OH as nitrogen source, DI water, 20 μL acetylacetone, and a drop of Triton TM X-100 into pastes followed by separately coating the resultant pastes via doctor blade method on the cleaned FTO glass sheets. The prepared undoped and N-doped TiO_2 films were dried and calcinated at 500°C for 30 minutes. The resultant films were separately soaked in 0.3 mM N719 dye solution, prepared by dissolving N719 dye in a mixture of acetonitrile and tert-butyl alcohol (50% v/v), for 12 h. After the dye-sensitization process, the photoanodes were washed with acetonitrile to remove the unanchored dye molecules and dried. Then, the corresponding devices were assembled by employing N719 dye-coated undoped or N-doped TiO_2 photoanode, I^-/I_3^- redox couple, and Pt-coated glass sheet as dye-sensitized photoanode, electrolyte, and counter electrode, respectively. Hereafter, the undoped TiO_2 shall be referred as pure TiO_2 and the N-doped TiO_2 with systematically varied N contents shall be referred as 10N-TiO_2, 20N-TiO_2, 30N-TiO_2, and 40N-TiO_2 with indication of the respective volumes of NH_4OH employed.

2.3. Characterization and Performance Evaluation.

The crystalline structures of the synthesized nanoparticles were analyzed using X-ray diffraction spectroscopy (XRD, PANalytical-AERIS, Almelo, Netherlands). The diffraction pattern was collected with Cu Kα radiation ($\lambda = 1.5408$ Å) under ambient temperature, through the following operational conditions: accelerated voltage of 40 kV, emission current of 44 mA, scan range (2θ) from 10° to 90° with a step size of 0.0027°, and a scan speed of 4°/min. The surface electron state of the N-doped TiO_2 was determined by X-ray photoelectron spectroscopy (XPS, Kratos Axis Ultra DLD). The surface characterization and elemental composition of the nanoparticles were studied by transmission electron microscope with an accelerating voltage of 120 kV (TEM, Hitachi HT7800) and scanning electron microscope (FESEM, Jeol JSM-7400F) along with energy-dispersive X-ray spectrometer (EDX). The Brunauer-Emmett-Teller (BET) model (Micromeritics Tristar 3000, at 77 K) was used to calculate the specific surface area. Pore size distribution of the nanoparticle was obtained from the desorption branch of the nitrogen isotherm through the Barrett-Joyner-Halenda (BJH) model. Absorption spectra of nanoparticles were recorded using a JENWAY 6800 UV-visible spectrophotometer (OSA, UK) which was controlled by Flight Deck software. The photovoltaic performances of all the fabricated devices with an effective area of 0.25 cm² were studied using Keithley-2400 source meter under simulated irradiation of 1 sun illumination intensity (100 mW/cm²) by 150 W Xe lamp with AM 1.5 filter (Peccell-PEC-L12, Kanagawa, Japan). Linear sweep voltammetry (LSV) and electrochemical impedance spectroscopy (EIS) measurements were performed using SP-150 electrochemical workstation (Biologic Science Instruments) through a two-electrode electrochemical setup.

3. Results and Discussion

3.1. Structural and Morphological Characterization of N-Doped TiO_2.

The crystal structures of the synthesized pure and N-doped TiO_2 nanoparticles were analyzed by XRD, and the corresponding XRD patterns are shown in Figure 1. The XRD patterns of all nanoparticles exhibit peaks at 25.20°, 37.60°, 48.20°, 53.70°, 55.00°, 62.50°, 68.50°, 70.20°, 74.89°, and 82.53° corresponding to the reflection planes of (101), (004), (200), (105), (211), (204), (116), (220), (215), and (224) which are consistent with the well-crystallized pure anatase TiO_2 phase (Anatase XRD JCPDS Card No. 21-1272) while peaks at 27.39°, 36.07°, and 41.2° correspond to the reflection planes of (110), (101), and (111) for rutile TiO_2 phase (Rutile JCPDS Card No. 21-1276).

The above observation confirms that no phase transition in TiO_2 had occurred due to N doping as both pure and N-doped TiO_2 nanoparticles exhibit similar anatase and rutile peaks. The crystallite sizes (d) of the nanoparticles were calculated by the Scherrer equation using the predominant anatase plane of (101) [13, 14]. The estimated crystallite sizes of the pure TiO_2, 10N-TiO_2, 20N-TiO_2, 30N-TiO_2, and 40N-TiO_2 nanoparticles were found to be 18.26, 17.60, 17.55, 17.50, and 17.12 nm, respectively. Trivial reduction observed in the crystallite size with increase in N content of the N-doped TiO_2 is in good agreement with the TEM images. Also, the observed insignificant variation in the crystallite size due to N doping on TiO_2 is consistent with the results reported by Kang et al. [18]. Further, the absence of

(a)

(b)

(c)

(d)
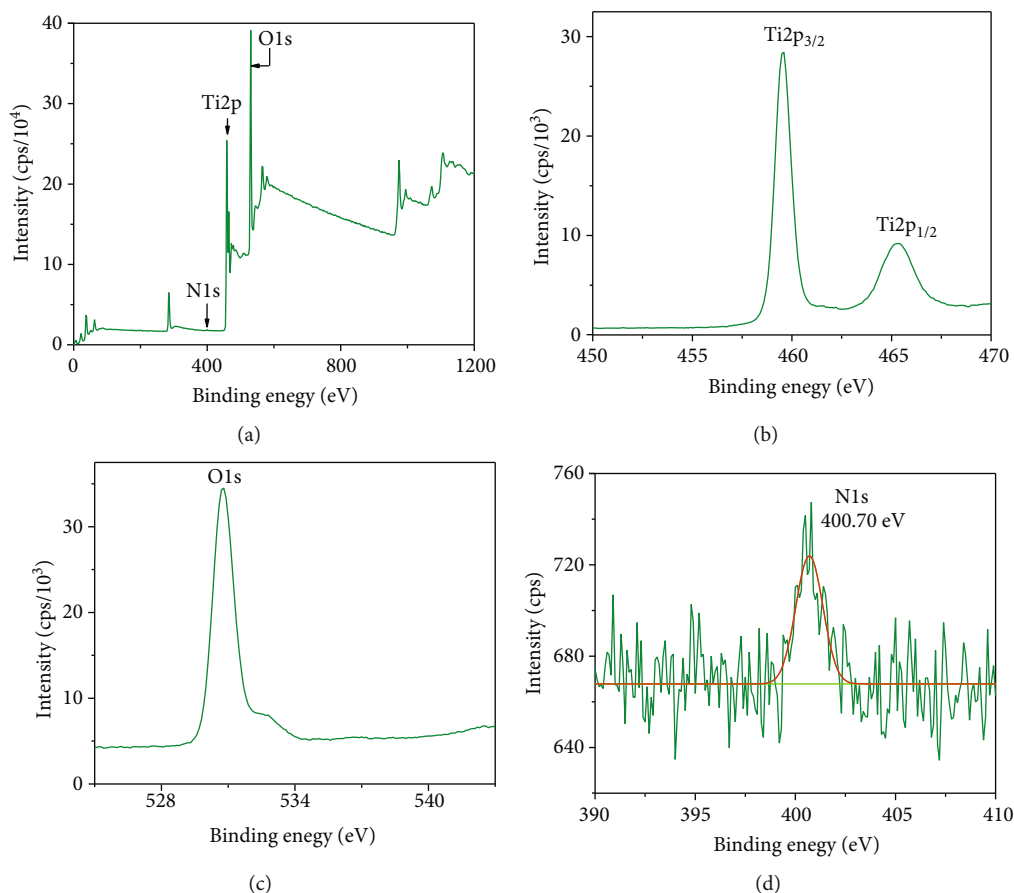
FIGURE 2: (a) XPS spectrum of 20N-TiO$_2$ and (b, c) high-resolution XPS spectra of Ti 2p, O 1s, and N 1s.

crystallite peaks representing nitrogen of N-doped TiO$_2$ in the XRD spectra may be attributed to the low N dopant quantities [30, 31]. Hence, XPS and EDX spectroscopic studies were performed to confirm the presence of nitrogen in the N-doped TiO$_2$ nanoparticles.

The surface chemical composition and oxidation states of 20N-TiO$_2$, as optimized sample, were studied and the findings are illustrated in Figure 2. The XPS survey reveals that the observed binding energies at 459.56 and 465.03 eV belong to the Ti 2p$_{3/2}$ and Ti 2p$_{1/2}$ spin-orbit splitting photoelectrons, respectively, which are consistent with the reported values for Ti^{4+} ion [32]. The binding energy at 529.6 eV of O 1s photoelectron confirms the presence of O^{2-} state in the nanoparticles. The literature on N 1s XPS peak analysis states that N doping on TiO$_2$ can occur in three different ways, namely, substitutional doping (replacement of O atom in the TiO$_2$ by N), interstitial doping (addition of N atom into the TiO$_2$ lattice), and atomic adsorption of N species [33, 34]. It is noteworthy to mention that though N doping on TiO$_2$ is reported in many literature, the exact assignment of N 1s XPS peak is still debatable. In addition, the binding energy of N 1s photoelectron highly depends on the method employed to synthesize the N-doped TiO$_2$ nanoparticles [35]. In the present study, N 1s peak observed at 400.7 eV could be attributed to the interstitial N of the N-doped TiO$_2$ with an O–Ti–N linkage [36] which is also in consistent with the XPS results of N-doped

TiO$_2$ reported by Liu et al. [37]. Moreover, the presence of this nitrogen in the N-doped TiO$_2$ has led to reduction of TiO$_2$ bandgap as well. Further, the EDX spectra (Figure S1 and Table S1) of pure TiO$_2$ and 20N-TiO$_2$ nanoparticles obtained in the binding energy region of 0.0-15.0 keV confirm the presence of N in the N-doped TiO$_2$ nanoparticles, and the EDX mapping of 20N-TiO$_2$ indicates that N ions are extensively and perfectly distributed on the surface of TiO$_2$.

The morphology and surface nature of the synthesized nanoparticles were studied using TEM and SEM techniques. As displayed in Figures 3(a)–3(c), the TEM images of pure TiO$_2$, 20N-TiO$_2$, and 40N-TiO$_2$ nanoparticles reveal that the synthesized nanoparticles are of spherical shape with the estimated particle size in the range of 18-20 nm. The said particle size values are in good agreement with the results obtained from the XRD measurements. Furthermore, formation of aggregates was observed in the structure of N-doped TiO$_2$ nanoparticles with high N content (40N-TiO$_2$). The high-resolution transmission electron microscopic (HRTEM) images of pure TiO$_2$ and 20N-TiO$_2$ (Figures 3(d) and 3(e)) show one set of lattice fringes with a space of 0.35 nm that could be indexed to the (101) plane of anatase phase. These results are consistent with the findings of the XRD analysis. However, significant fringe lattice associated with the nitrogen of N-doped TiO$_2$ is not observed due to the small quantity of the N dopant.
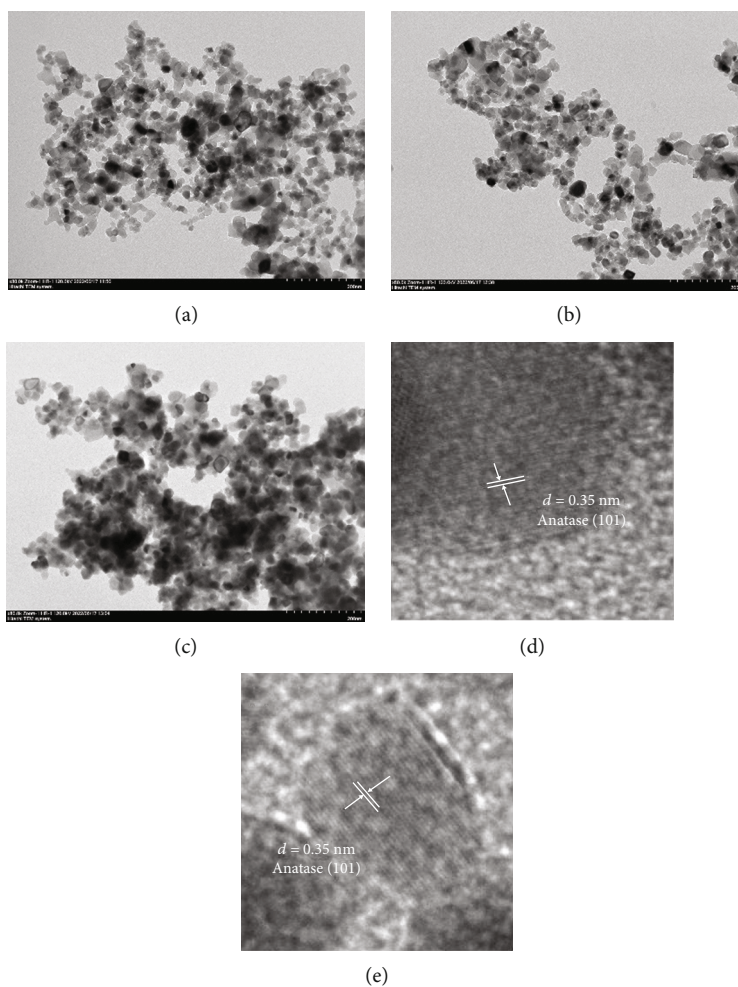
FIGURE 3: TEM images of (a) pure TiO_2, (b) 20N-TiO_2, and (c) 40N-TiO_2 nanoparticles; HRTEM images of (d) pure TiO_2 and (e) 20N-TiO_2.
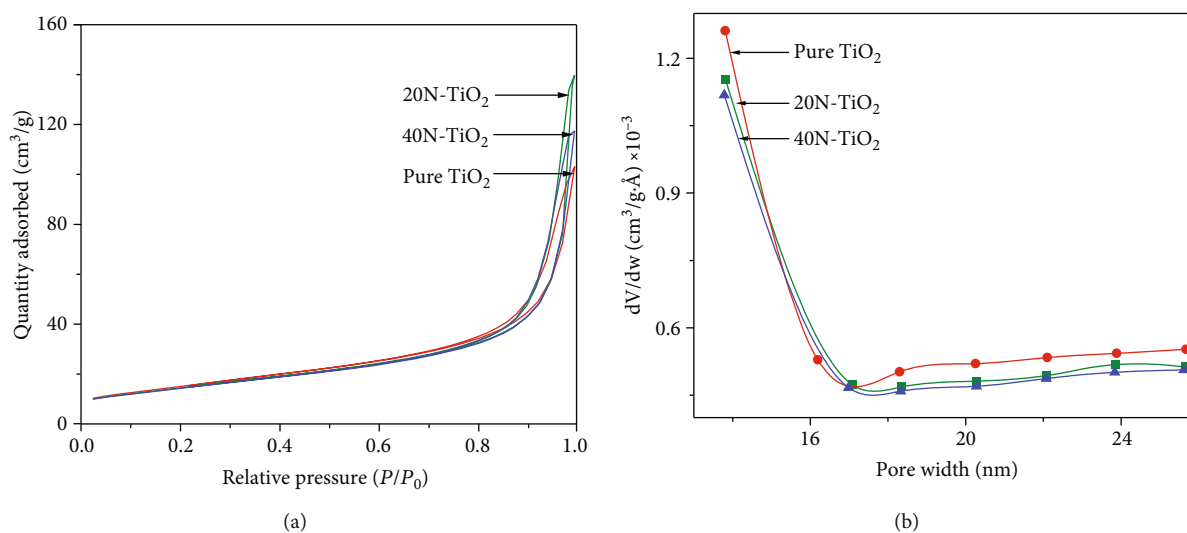
FIGURE 4: (a) Nitrogen adsorption-desorption isotherms and (b) pore size distribution curves of pure TiO_2, 20N-TiO_2, and 40N-TiO_2.

The SEM images of pure TiO_2, 10N-TiO_2, 20N-TiO_2, 30N-TiO_2, and 40N-TiO_2 nanoparticles, shown in Figure S2 (a-e), reveal that all nanoparticles are in uniform spherical shape and N doping had not caused any morphological changes. Similar observation is reported by Lin et al. for N-doped TiO_2 using ammonium hydroxide as

(a)

(b)
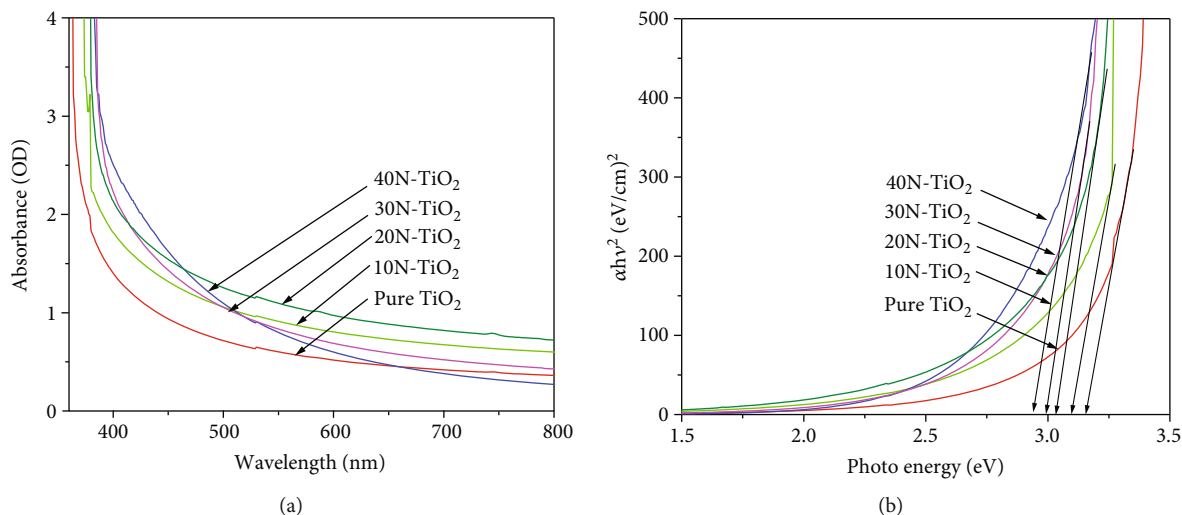
Figure 5: (a) UV-visible absorption spectra of pure TiO_2, 10N-TiO_2, 20N-TiO_2, 30N-TiO_2, and 40N-TiO_2 nanoparticles and (b) Tauc plot of the corresponding nanoparticles.

(a)

(b)
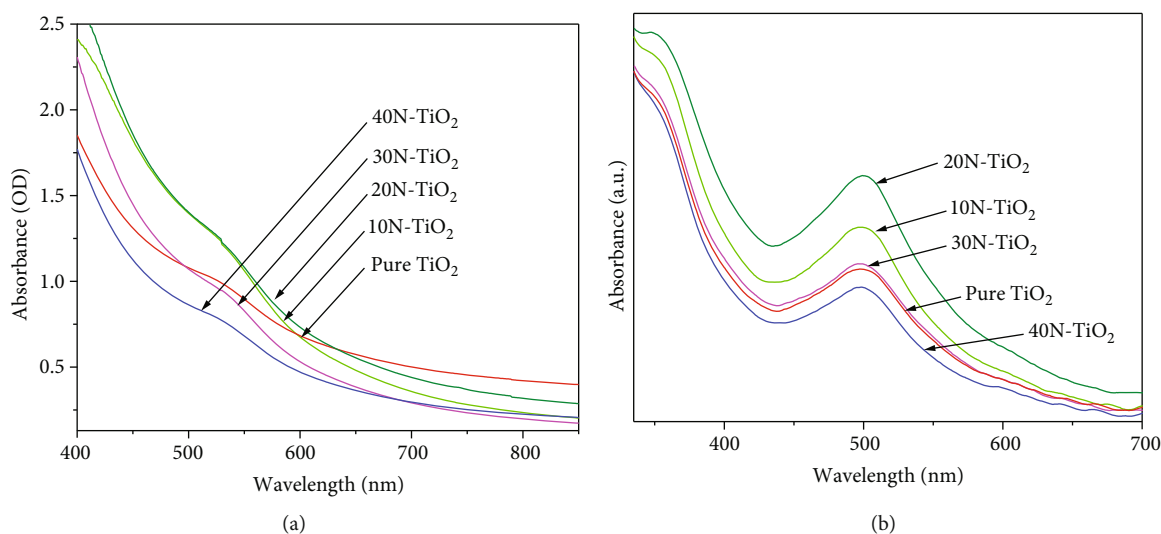
Figure 6: UV-visible absorption spectra of (a) dye-coated pure TiO_2, 10N-TiO_2, 20N-TiO_2, 30N-TiO_2, and 40N-TiO_2 films and (b) desorbed dye from the same films.

nitrogen source [38]. Further, Figure S2 (d and e) clearly exhibits that particles start to agglomerate when higher quantities of N dopant are used and consequently the surface area and pore size distribution of the nanoparticles get affected. The Brunauer-Emmett-Teller (BET) and Barrett-Joyner-Halenda (BJH) measurements were carried out to investigate the surface area and pore size distribution of the nanoparticles, respectively.

Figure 4 shows the nitrogen adsorption-desorption isotherms and the corresponding pore size distribution curves of the pure TiO_2, 20N-TiO_2, and 40N-TiO_2 nanoparticles. As it is observed in Figure 4(a), all three nanoparticles exhibit a IV type isotherm curve according to the IUPAC classification [39]. As per the IUPAC nomenclature, the pore size of a mesoporous material varies between 2 and 50 nm. The wide distribution of pore size/width in the range of

10–30 nm observed for the synthesized nanomaterial is depicted in Figure 4(b), which indicates its' mesoporous structure [40]. The BET surface areas of pure TiO_2, 20N-TiO_2, and 40N-TiO_2 nanoparticles were found to be 57.92, 53.28, and 51.97 m^2g^{-1}, respectively. Hence, the BET analysis reveals that the surface area of the synthesized nanoparticles is mainly controlled by the size of TiO_2 though trivial changes occur due to N doping as already confirmed by the XRD and TEM measurements [41]. The average adsorption pore diameters of pure TiO_2, 20N-TiO_2, and 40N-TiO_2 nanoparticles were found to be 10.65, 15.99, and 13.52 nm, respectively. The observed optimum value for 20N-TiO_2 confirms that N doping, to a certain extent, not only modifies the surface area but also extremely enhances the pore size of the nanoparticles. However, further increase in the N dopant (e.g., 40N-TiO_2) leads to reduction in both surface

(a)

(b)
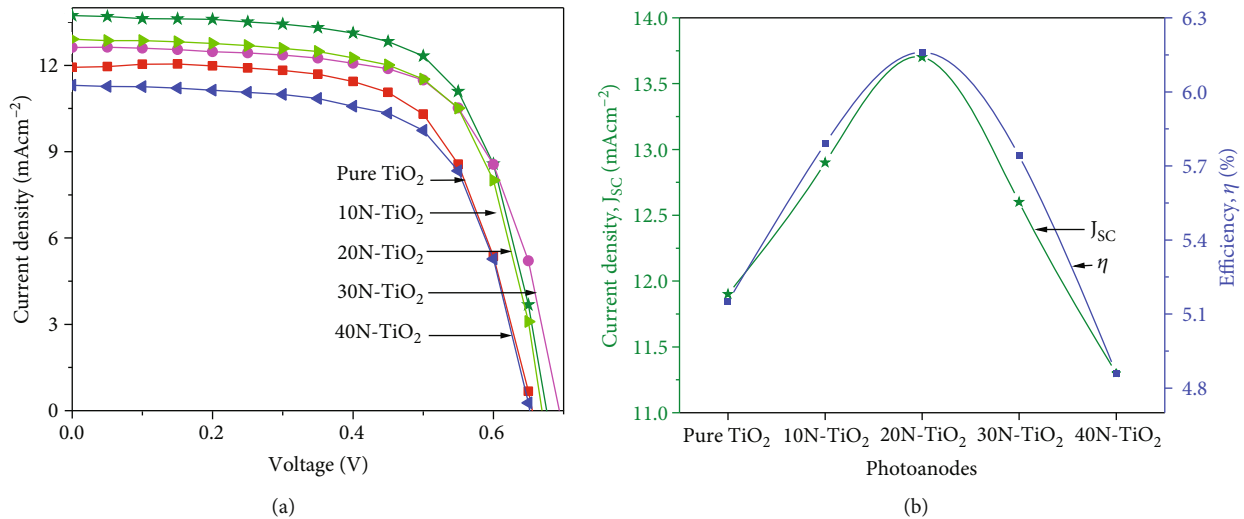
FIGURE 7: (a) Current-voltage (J-V) characteristics of the DSSCs assembled with pure TiO_2, 10N-TiO_2, 20N-TiO_2, 30N-TiO_2, and 40N-TiO_2 photoanodes tested under simulated irradiation of intensity 100 mW cm^{-2} with AM 1.5 filter and (b) variation in J_{SC} and efficiency with different amounts of N dopant.

TABLE 1: Summary of photovoltaic parameters of the DSSCs assembled with pure TiO_2, 10N-TiO_2, 20N-TiO_2, 30N-TiO_2, and 40N-TiO_2 photoanodes.

Photoanode	J_{SC} (mA/cm^2)	V_{OC} (V)	FF	PCE, η (%)
Pure TiO_2	11.90	0.65	0.65	5.15
10N-TiO_2	12.90	0.67	0.67	5.79
20N-TiO_2	13.70	0.67	0.66	6.16
30N-TiO_2	12.60	0.69	0.66	5.74
40N-TiO_2	11.30	0.65	0.66	4.86

area and average adsorption pore diameter due to agglomeration of particles as observed in the corresponding TEM and SEM images. It is well-known that pore size improvement without sacrificing the surface area is beneficial as it allows a higher number of dye and electrolyte molecules to fill the pores of TiO_2 film which in turn would enhance the short circuit current density of the device [42].

3.2. Optical Characterization of N-Doped TiO_2.
An optical study, utilizing UV-visible spectrophotometer, was performed to measure the light absorption capacities and estimate bandgaps of pure TiO_2, 10N-TiO_2, 20N-TiO_2, 30N-TiO_2, and 40N-TiO_2 nanoparticles (Figures 5(a) and 5(b)).

The N-doped TiO_2 nanoparticles showed a gradual shift in the UV-visible region to longer wavelengths (red shift) with an increase in the amount of N dopant compared to pure TiO_2 (Figure 5(a)). This observation is in consistent with the previously reported studies [18, 38, 43]. Further, the estimated bandgaps of the said nanoparticles, calculated by Tauc plot as reported in our previous study [14], were found to be 3.15, 3.10, 3.03, 2.99, and 2.94 eV for pure TiO_2, 10N-TiO_2, 20N-TiO_2, 30N-TiO_2, and 40N-TiO_2 nanoparticles, respectively (Figure 5(b)). This reduction in the bandgap as a result of N doping could have been caused by either formation of isolated narrow bands above the valance band of TiO_2 by mixing the 2p states of N and O in the dopant and TiO_2, respectively (interstitial doping) [44] or replacement of oxygen-deficient sites by the nitrogen (substitutional doping) [43]. However, no peak for substitutional nitrogen was detected in the XPS study. Hence, the reduction in the bandgap could be attributed to the impurity levels formed above the valance band of TiO_2 due to the interstitial nitrogen doping. Also, it has been reported that interstitial doping by nitrogen extensively influences and reduces the bandgap of TiO_2 compared to substitutional N doping [45].

Further, the effect of N doping on dye adsorption as well as desorption was studied. Initially, pure TiO_2-, 10N-TiO_2-, 20N-TiO_2-, 30N-TiO_2-, and 40N-TiO_2-coated films were soaked in the N719 dye overnight, and the resultant dye-coated films were analyzed by UV-visible spectroscopy (Figure 6(a)). Then, the same photoanodes were dipped in 5 mL of 1 N NaOH solution, and the desorbed dye in NaOH solution was subjected to UV-visible spectroscopic analysis (Figure 6(b)).

As shown in Figure 6, enhanced light absorption was observed for dye-coated N-doped TiO_2 films, and the maximum light absorption was obtained for the dye-coated 20N-TiO_2 film. The improved light absorption of dye-coated N-doped TiO_2 films could be attributed to the increased pore size for dye adsorption as a result of N doping which was confirmed by the BET and BJH studies. The greater dye adsorption on N-doped TiO_2 film due to the increased porosity of TiO_2 by N doping has been reported earlier as well [46]. However, a further increase in the amount of N dopant reduces light absorption due to agglomeration of the particles giving rise to a reduction in dye adsorption. These observations are in good agreement with the J_{SC} values of the corresponding devices fabricated from the above dye-coated N-doped TiO_2 films.

3.3. Performance Evaluation of DSSCs.
The photovoltaic performance of the N719 dye-coated pure TiO_2, 10N-TiO_2, 20N-TiO_2, 30N-TiO_2, and 40N-TiO_2 photoanodes was

TABLE 2: Comparison of the PCEs of N-doped P25-TiO$_2$ photoanode-based devices.

Doping method and N source	Device active area (cm^{-2})	Dye	Additional modification	Counter electrode	PCE, η (%)	Ref.
Grinding P25-TiO$_2$ and urea for 30 min in a mortar and annealing at 400°C for 1 hr	0.50	N719	—	Pt	2.93	[47]
Grinding P25-TiO$_2$ and thiourea for 30 min in a mortar and annealing at 400°C for 1 hr	0.50	N719	(i) N codoped with S	Pt	3.35	[48]
Sol-gel process with electrospinning	0.25	N719	(i) N-doped TiO$_2$ nanofiber photoanode	Pt	4.70	[27]
Sol-gel process	0.25		—	Pt	4.86	[18]
Ball milling method (urea as N source)	0.16	N3	—	Pt	6.71	[49]
Wet method	0.16	N719	(i) Use of screen-printing technique to fabricate TiO$_2$ film (ii) TiCl$_4$ treatment (iii) Nanostructured photoanode	Pt	7.27	[28]
Wet method	0.16	N719	(i) Use of screen-printing technique to fabricate TiO$_2$ film (ii) TiCl$_4$ treatment	Pt	8.32	[25]
Sintering P25-TiO$_2$ at 500°C for 3 h under dry N$_2$ and NH$_3$ gas flow	0.16	N719	(i) A screen-printing technique was used to fabricate the TiO$_2$ films (ii) TiCl$_4$ treatment (iii) Modified I^-/I_3^- electrolyte used	Pt	8.00	[50]
Solid-state reaction method (NH$_4$OH as N source)	0.25	N719	—	Pt	6.16	This work
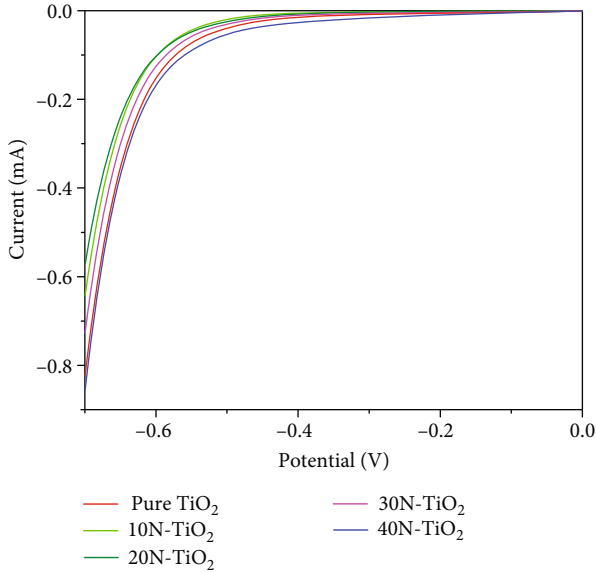
FIGURE 8: LSV measurements of the DSSCs assembled with pure TiO$_2$, 10N-TiO$_2$, 20N-TiO$_2$, 30N-TiO$_2$, and 40N-TiO$_2$ photoanodes under the dark condition.

studied using I^-/I_3^- electrolyte and Pt counter electrode under the simulated irradiation with 100 mW cm^{-2} and AM 1.5 filter, and the results are depicted in Figure 7(a) and the PV parameters are summarized in Table 1.

The J-V studies revealed that the PCE of N-doped TiO$_2$-based DSSCs slightly improved because of marginal increase in FF (fill factor) and V_{OC} (open circuit voltage) and considerable increase in J_{SC} (short circuit current). It was observed that when the amount of N dopant had been increased from 0 to 20 μL, the J_{SC} enhanced significantly from 11.90 to 13.70 mA/cm^2; but, a further increase in the N dopant amount resulted in a downward trend with respect to J_{SC} (11.30 mA/cm^2 for 40N-TiO$_2$). Figure 7(b) indicates the influence of different amounts of N dopant on J_{SC} and η. The variation in J_{SC} values could be attributed to the modified surface properties of N-doped TiO$_2$ as explained earlier. The observed reduction in J_{SC} and PCE beyond 20N-TiO$_2$ could have been caused by decreased dye adsorption due to the particle agglomeration. In the present study, the device fabricated with 20N-TiO$_2$ electrode showed the best η of 6.16%, which was 20% higher than that of the pure TiO$_2$-based DSSC ($\eta = 5.15\%$).

Table 2 compares the PCE of the N-doped P25-TiO$_2$ photoanode-based devices. Although the experimental conditions and other factors vary, based on the summary of the table, our proposed synthesized N-doped P25-TiO$_2$ nanomaterial is shown to be more efficient for the DSSC application.

Moreover, charge recombination of the injected electrons in the CB of TiO$_2$ with either the oxidized dye or the oxidized form of the electrolyte species is another limiting factor in the DSSCs' performance. To investigate the impact of N doping on the recombination mechanism of DSSCs, linear sweep voltammetry (LSV) and electrochemical impedance spectroscopic (EIS) measurements were carried out in dark.
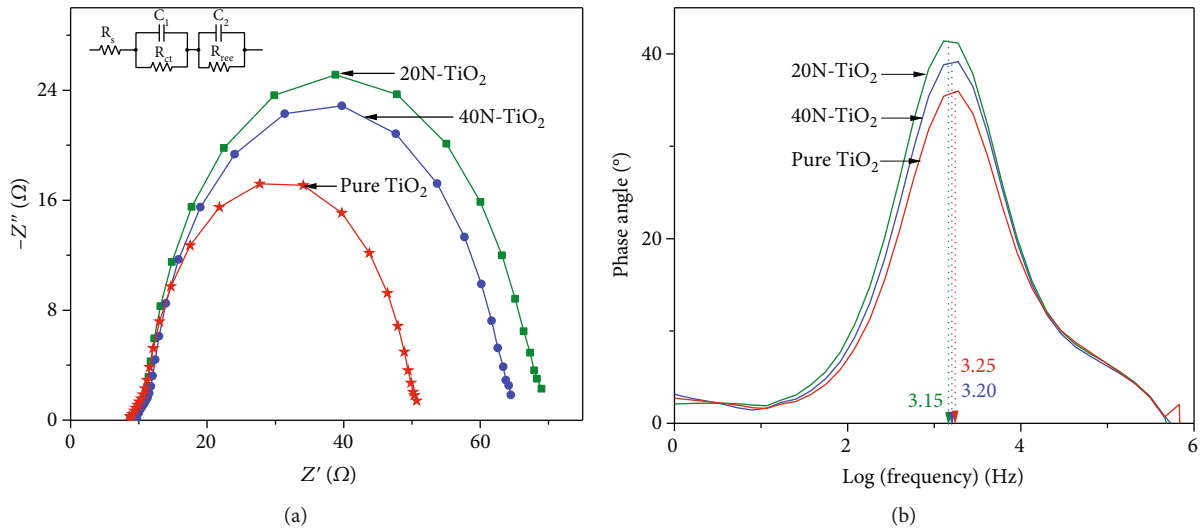
FIGURE 9: (a) Nyquist plots of the DSSCs assembled with pure TiO$_2$, 20N-TiO$_2$, and 40N-TiO$_2$ photoanodes tested under the dark condition and (b) bode plots of the same devices.

TABLE 3: Summary of EIS parameters of the DSSCs assembled with pure TiO$_2$, 20N-TiO$_2$, and 40N-TiO$_2$ photoanodes.

Photoanode	R_s	R_{ct}	R_{rec}	f_{max} (Hz)	T_e (ms)
Pure TiO$_2$	9.01	1.78	39.39	3.25	48.97
20N-TiO$_2$	9.36	1.56	56.84	3.15	50.52
40N-TiO$_2$	9.90	1.57	52.03	3.20	49.73

Figure 8 illustrates the LSV measurements of the pure TiO$_2$ and N-doped TiO$_2$-based devices on application of a negative potential between the photoanode and the counter electrode. When a negative potential is applied between the photoanode and the counter electrode, the electrons get transferred under the electric field while undergoing different recombination pathways. As such, the higher recombination rate causes large dark current in the TiO$_2$/dye/electrolyte interface while the smaller recombination rate gives rise to lower dark current. In the present study, reduced dark current values were found for the devices assembled with 10N-TiO$_2$ and 20N-TiO$_2$ photoanodes. This could be attributed to the formation of O-Ti-N bond which would have suppressed the reduction of I_3^- on the TiO$_2$ electrode [51]. But, further increase in the amount of N dopant up to 40 μL enhanced the dark current which may be due to the recombination reaction caused by excessive insertion of nitrogen dopant in the TiO$_2$ lattice.

Another technique, which is widely employed to investigate the charge transport resistance at each interface in the DSSCs, is electrochemical impedance spectroscopy (EIS). In the present study, the measurements were carried out at a frequency range from 10^{-2} to 10^6 Hz, as well as keeping V_{OC} as the bias voltage in dark. A typical electrochemical impedance spectrum consists of three semicircles intersecting at the X axis of which the smallest semicircle is known as series resistance (R_s) and related to the sheet resistance on the transparent conductive oxide (TCO) substrate and the contact resistance between TCO and TiO$_2$; the semicircle in the higher frequency region is responsible for the charge transfer resistance at the electrolyte/Pt electrode interface (R_{ct}); and the largest semicircle corresponds to the electron transfer at the TiO$_2$/dye/electrolyte interface and is referred as charge recombination resistance in dark condition (R_{rec}) [13, 14, 52]. Figure 9(a) shows the Nyquist plots of the DSSCs assembled with pure TiO$_2$, 20N-TiO$_2$, and 40N-TiO$_2$ photoanodes, and the respective EIS parameters are summarized in Table 3.

As reported in Table 3, charge recombination resistances (R_{rec}) of pure TiO$_2$, 20N-TiO$_2$, and 40N-TiO$_2$ photoanode-based DSSCs were found to be 39.39, 56.84, and 52.03 Ω, respectively. The DSSC assembled with 20N-TiO$_2$ exhibited the highest charge recombination resistance (R_{rec}) indicating that recombination rate is retarded when appropriate amount of nitrogen is doped into TiO$_2$. However, further insertion of nitrogen into TiO$_2$ (40N-TiO$_2$) lowered the R_{rec} value due to enhanced recombination. Figure 9(b) illustrates the bode plots of the pure TiO$_2$, 20N-TiO$_2$, and 40N-TiO$_2$ photoanode-based devices, and the electron life time (T_e), which is also referred as the charge recombination time under the dark condition, was estimated using the following equation:

$$T_e = \frac{1}{2\pi f_{max}},$$ (1)

where f_{max} is the maximum frequency corresponding to the peak [53]. In the present study, slight variations in the charge recombination time were observed among the tested devices and the one with 20N-TiO$_2$ photoanode exhibited the highest T_e value reconfirming that recombination rate is retarded. Also, excessive insertion of nitrogen dopant into the TiO$_2$ decreased charge recombination time and thereby facilitated the recombination reaction. The said results are consistent with the LSV findings. Further, it has been reported in the literature that incorporation of huge numbers of nitrogen atom

on the TiO_2 lattice or existence of inactive nitrogen atoms can generate trap states around the Fermi levels and assist the recombination process [18, 34]. The results of this study reveal that the performance of N-doped DSSCs is significantly influenced by the dye uptake ability rather than the charge transport resistance of the said devices.

4. Conclusion

In the present study, N-doped TiO_2 nanoparticles with systematically varied amounts of NH_4OH were successfully synthesized by a facile solid-state reaction, characterized and effectively integrated in the fabrication of DSSCs. XRD patterns of the synthesized nanoparticles suggested that N doping had not altered the TiO_2 anatase and rutile crystal structures. The presence of nitrogen in the N-doped TiO_2 nanoparticles was confirmed by XPS and EDX analyses. SEM and TEM images showed that high amount of N dopant had resulted in the agglomeration of nanoparticles. BET, BJH, and UV-visible spectroscopic results revealed that optimum amount of N doping on TiO_2 increases the pore diameter of TiO_2 particles which leads to higher dye adsorption. Through the J-V measurement, it was found that the device assembled with 20N-TiO_2 photoanode possessed 20% higher PCE ($\eta = 6.16\%$) compared to the control device ($\eta = 5.15\%$) mainly due to enhanced J_{SC}. This improvement in J_{SC} value of the optimised device could be attributed predominately to the enhanced visible light harvest as a result of increased dye uptake along with a trivial contribution from the reduced charge recombination process. Among the reported studies on DSSCs based on the N-doped P25-TiO_2 photoanodes, our method gives the best PCEs for the DSSCs.

Data Availability

All of the data supporting underlying findings are included in the manuscript and its supplemental files.

Conflicts of Interest

The authors declare no conflict of interest.

Authors' Contributions

Tharmakularasa Rajaramanan was responsible for conceptualization, methodology, data curation, software, and writing the original draft preparation. Fatemeh Heidari Gourji performed data curation and investigation and reviewed and edited the manuscript. Dhayalan Velauthapillai was responsible for data curation, investigation, validation, supervision, funding acquisition, reviewing, and editing. Punniamoorthy Ravirajan was responsible for data curation, investigation, validation, supervision, funding acquisition, reviewing, and editing. Meena Senthilnanthanan was responsible for data curation, investigation, validation, supervision, visualization, reviewing, and editing.

Supplementary Materials

The presence of N in the optimized 20N-TiO_2 nanoparticles was further confirmed by EDX analysis, as shown in Figure S1 (a, b). The summary of EDX results, presented in Table S1, confirms that the amount of N doped in 20N-TiO_2 nanoparticles is in compliance with the distribution of N dopant in the same as shown in the EDX mapping (Figure S1 (c, d)). Figure S1: EDX spectra of (a) pure TiO_2 and (b) 20N-TiO_2; EDX mapping of (c) pure TiO_2 and (d) 20N-TiO_2. Table S1: weight percentage of pure TiO_2 and 20N-TiO_2 in terms of energy dispersive X-ray spectroscopic investigation. Figure S2 depicts the SEM analyses of pure TiO_2, 10N-TiO_2, 20N-TiO_2, 30N-TiO_2, and 40N-TiO_2 nanoparticles. The results reveal that the pure and N-doped TiO_2 possess uniform spherical shape and particle aggregation occurs at high N doping (Figure S2 (d, e)). Figure S2: SEM images of (a) pure TiO_2, (b-e) 10N-TiO_2, 20N-TiO_2, 30N-TiO_2, and 40N-TiO_2 nanoparticles. *(Supplementary Materials)*

References

[1] A. Pirashanthan, M. Thanihaichelvan, K. Mariappan, D. Velauthapillai, P. Ravirajan, and Y. Shivatharsiny, "Synthesis of a carboxylic acid-based ruthenium sensitizer and its applicability towards dye-sensitized solar cells," *Solar Energy*, vol. 225, pp. 399–406, 2021.

[2] T. Kajana, A. Pirashanthan, A. Yuvapragasam, D. Velauthapillai, P. Ravirajan, and M. Senthilnanthanan, "Bimetallic AC/Ag_2CrO_4/SnS heterostructure photoanode for energy conversion and storage: a self-powered photocapacitor," *Journal of Power Sources*, vol. 520, article 230883, 2022.

[3] V. S. Manikandan, A. K. Palai, S. Mohanty, and S. K. Nayak, "Eosin-Y sensitized core-shell TiO_2-ZnO nano-structured photoanodes for dye-sensitized solar cell applications," *Journal of Photochemistry and Photobiology B: Biology*, vol. 183, pp. 397–404, 2018.

[4] M. Ye, X. Wen, M. Wang et al., "Recent advances in dye-sensitized solar cells: from photoanodes, sensitizers and electrolytes to counter electrodes," *Materials Today*, vol. 18, no. 3, pp. 155–162, 2015.

[5] D. Kishore Kumar, J. Kříž, N. Bennett et al., "Functionalized metal oxide nanoparticles for efficient dye-sensitized solar cells (DSSCs): a review," *Materials Science for Energy Technologies*, vol. 3, pp. 472–481, 2020.

[6] K. Basu, D. Benetti, H. Zhao et al., "Enhanced photovoltaic properties in dye sensitized solar cells by surface treatment of SnO_2 photoanodes," *Scientific Reports*, vol. 6, no. 1, article 23312, 2016.

[7] W. Wanninayake, K. Premaratne, and R. Rajapakse, "Enhancing performance of SnO_2-based dye-sensitized solar cells using

ZnO passivation layer," *International Journal of Photoenergy*, vol. 2016, Article ID 9087478, 8 pages, 2016.

[8] A. K. Chandiran, M. Abdi-Jalebi, M. K. Nazeeruddin, and M. Grätzel, "Analysis of electron transfer properties of ZnO and TiO_2 photoanodes for dye-sensitized solar cells," *ACS Nano*, vol. 8, no. 3, pp. 2261–2268, 2014.

[9] M. Giannouli, K. Govatsi, G. Syrrokostas, S. Yannopoulos, and G. Leftheriotis, "Factors affecting the power conversion efficiency in ZnO DSSCs: nanowire vs. nanoparticles," *Materials*, vol. 11, no. 3, p. 411, 2018.

[10] K. Prabakaran, S. Mohanty, and S. K. Nayak, "Solid state dye sensitized solar cells: eosin-Y sensitized TiO_2-ZnO/PEO-PVDF-HFP-MMT electrolytes/MWCNT-Nafion® counter electrode," *Ceramics International*, vol. 41, no. 9, pp. 11824–11835, 2015.

[11] A. Kay and M. Grätzel, "Dye-sensitized core–shell nanocrystals: improved efficiency of mesoporous tin oxide electrodes coated with a thin layer of an insulating oxide," *Chemistry of Materials*, vol. 14, no. 7, pp. 2930–2935, 2002.

[12] S. Shanmugaratnam, B. Selvaratnam, A. Baride et al., "SnS_2/TiO_2 nanocomposites for hydrogen production and photodegradation under extended solar irradiation," *Catalysts*, vol. 11, no. 5, p. 589, 2021.

[13] T. Rajaramanan, S. Shanmugaratnam, V. Gurunanthanan et al., "Cost effective solvothermal method to synthesize Zn-doped TiO_2 nanomaterials for photovoltaic and photocatalytic degradation applications," *Catalysts*, vol. 11, no. 6, p. 690, 2021.

[14] T. Rajaramanan, M. Natarajan, P. Ravirajan, M. Senthilnanthanan, and D. Velauthapillai, "Ruthenium (Ru) doped titanium dioxide (P25) electrode for dye sensitized solar cells," *Energies*, vol. 13, no. 7, p. 1532, 2020.

[15] B. Roose, S. Pathak, and U. Steiner, "Doping of TiO_2 for sensitized solar cells," *Chemical Society Reviews*, vol. 44, no. 22, pp. 8326–8349, 2015.

[16] K. Subalakshmi and J. Senthilselvan, "Effect of fluorine-doped TiO_2 photoanode on electron transport, recombination dynamics and improved DSSC efficiency," *Solar Energy*, vol. 171, pp. 914–928, 2018.

[17] F. Huang, A. Yan, and H. Zhao, "Influences of doping on photocatalytic properties of TiO_2 photocatalyst," *Semiconductor Photocatalysis-Materials, Mechanisms and Applications*, pp. 31–80, 2016.

[18] S. H. Kang, H. S. Kim, J.-Y. Kim, and Y.-E. Sung, "Enhanced photocurrent of nitrogen-doped TiO_2 film for dye-sensitized solar cells," *Materials Chemistry and Physics*, vol. 124, no. 1, pp. 422–426, 2010.

[19] V. Madurai Ramakrishnan, M. Natarajan, S. Pitchaiya, A. Santhanam, D. Velauthapillai, and A. Pugazhendhi, "Microwave assisted solvothermal synthesis of quasi cubic F doped TiO_2 nanostructures and its performance as dye sensitized solar cell photoanode," *International Journal of Energy Research*, vol. 45, no. 12, pp. 17259–17268, 2021.

[20] S. K. Park, J. S. Jeong, T. K. Yun, and J. Y. Bae, "Preparation of carbon-doped TiO_2 and its application as a photoelectrodes in dye-sensitized solar cells," *Journal of Nanoscience and Nanotechnology*, vol. 15, no. 2, pp. 1529–1532, 2015.

[21] Q. Sun, J. Zhang, P. Wang et al., "Sulfur-doped TiO_2 nanocrystalline photoanodes for dye-sensitized solar cells," *Journal of Renewable and Sustainable Energy*, vol. 4, no. 2, article 023104, 2012.

[22] H. Tian, L. Hu, C. Zhang et al., "Enhanced photovoltaic performance of dye-sensitized solar cells using a highly crystallized mesoporous TiO_2 electrode modified by boron doping," *Journal of Materials Chemistry*, vol. 21, no. 3, pp. 863–868, 2011.

[23] Q. Hou, Y. Zheng, J.-F. Chen, W. Zhou, J. Deng, and X. Tao, "Visible-light-response iodine-doped titanium dioxide nanocrystals for dye-sensitized solar cells," *Journal of Materials Chemistry*, vol. 21, no. 11, pp. 3877–3883, 2011.

[24] R. Asahi, T. Morikawa, T. Ohwaki, K. Aoki, and Y. Taga, "Visible-light photocatalysis in nitrogen-doped titanium oxides," *Science*, vol. 293, no. 5528, pp. 269–271, 2001.

[25] W. Guo, Y. Shen, G. Boschloo, A. Hagfeldt, and T. Ma, "Influence of nitrogen dopants on N-doped TiO_2 electrodes and their applications in dye-sensitized solar cells," *Electrochimica Acta*, vol. 56, no. 12, pp. 4611–4617, 2011.

[26] T. Ma, M. Akiyama, E. Abe, and I. Imai, "High-efficiency dye-sensitized solar cell based on a nitrogen-doped nanostructured titania electrode," *Nano Letters*, vol. 5, no. 12, pp. 2543–2547, 2005.

[27] M. Motlak, M. S. Akhtar, N. A. M. Barakat, A. M. Hamza, O. B. Yang, and H. Y. Kim, "High-efficiency electrode based on nitrogen-doped TiO_2 nanofibers for dye-sensitized solar cells," *Electrochimica Acta*, vol. 115, pp. 493–498, 2014.

[28] W. Guo, Y. Shen, L. Wu, Y. Gao, and T. Ma, "Effect of N dopant amount on the performance of dye-sensitized solar cells based on N-doped TiO_2 electrodes," *The Journal of Physical Chemistry C*, vol. 115, no. 43, pp. 21494–21499, 2011.

[29] R. Kushwaha, R. Chauhan, P. Srivastava, and L. Bahadur, "Synthesis and characterization of nitrogen-doped TiO_2 samples and their application as thin film electrodes in dye-sensitized solar cells," *Journal of Solid State Electrochemistry*, vol. 19, no. 2, pp. 507–517, 2015.

[30] M. S. Azami, W. I. Nawawi, A. H. Jawad, M. A. M. Ishak, and K. Ismail, "N-doped TiO_2 synthesised via microwave induced photocatalytic on RR_4 dye removal under LED light irradiation," *Sains Malays*, vol. 46, no. 8, pp. 1309–1316, 2017.

[31] F. Peng, L. Cai, L. Huang, H. Yu, and H. Wang, "Preparation of nitrogen-doped titanium dioxide with visible-light photocatalytic activity using a facile hydrothermal method," *Journal of Physics and Chemistry of Solids*, vol. 69, no. 7, pp. 1657–1664, 2008.

[32] H. Lee and M. Kang, "Synthesis of N-doped TiO_2 particles from aquaethylenediaminetitanium(IV) hydroxide complex and their optical properties on dye-sensitized solar cells," *Journal of Sol-Gel Science and Technology*, vol. 69, no. 2, pp. 325–337, 2014.

[33] H. Abdullah, M. M. R. Khan, H. R. Ong, and Z. Yaakob, "Modified TiO_2 photocatalyst for CO_2 photocatalytic reduction: an overview," *Journal of CO2 Utilization*, vol. 22, pp. 15–32, 2017.

[34] J. Wang, K. Tapio, A. Habert et al., "Influence of nitrogen doping on device operation for TiO2-based solid-state dye-sensitized solar cells: photo-physics from materials to devices," *Nanomaterials*, vol. 6, no. 3, p. 35, 2016.

[35] X. Qiu and C. Burda, "Chemically synthesized nitrogen-doped metal oxide nanoparticles," *Chemical Physics*, vol. 339, no. 1, pp. 3–10, 2007.

[36] Y. Zhang, F. du, X. Yan et al., "Improvements in the electrochemical kinetic properties and rate capability of anatase titanium dioxide nanoparticles by nitrogen doping," *ACS Applied Materials & Interfaces*, vol. 6, no. 6, pp. 4458–4465, 2014.

[37] J. Liu, X. Li, H. Hou, and M. Zhou, "Facile synthesis of anatase–rutile diphase N-doped TiO_2 nanoparticles with excellent visible light photocatalytic activity," *Catalysts*, vol. 10, no. 10, p. 1126, 2020.

[38] Y.-H. Lin, C.-H. Weng, A. L. Srivastav, Y.-T. Lin, and J.-H. Tzeng, "Facile synthesis and characterization of N-doped TiO_2 photocatalyst and its visible-light activity for photooxidation of ethylene," *Journal of Nanomaterials*, vol. 2015, Article ID 807394, 10 pages, 2015.

[39] Z. A. ALOthman, "A review: fundamental aspects of silicate mesoporous materials," *Materials*, vol. 5, no. 12, pp. 2874–2902, 2012.

[40] F. Heidari Gourji, D. Velauthapillai, and M. Keykhaei, "Ultra-ordered array of $CuCo_2S_4$ microspheres on co-doped nitrogen, sulfur-porous graphene sheets with superior electrochemical performance for supercapacitor application," *Energy Reports*, vol. 8, pp. 7712–7723, 2022.

[41] H.-L. Hsu, C.-F. Tien, and J. Leu, "Effect of pore size/distribution in TiO2 films on agarose gel electrolyte-based dye-sensitized solar cells," *Journal of Solid State Electrochemistry*, vol. 18, no. 6, pp. 1665–1671, 2014.

[42] W. Song, Y. Gong, J. Tian, G. Cao, H. Zhao, and C. Sun, "Novel photoanode for dye-sensitized solar cells with enhanced light-harvesting and electron-collection efficiency," *ACS Applied Materials & Interfaces*, vol. 8, no. 21, pp. 13418–13425, 2016.

[43] W. Qin, S. Lu, X. Wu, and S. Wang, "Dye-sensitized solar cell based on N-doped TiO_2 electrodes prepared on titanium," *International Journal of Electrochemical Science*, vol. 8, no. 6, pp. 7984–7990, 2013.

[44] S. Sato, R. Nakamura, and S. Abe, "Visible-light sensitization of TiO_2 photocatalysts by wet-method N doping," *Applied Catalysis A: General*, vol. 284, no. 1-2, pp. 131–137, 2005.

[45] S. A. Ansari, M. M. Khan, M. O. Ansari, and M. H. Cho, "Nitrogen-doped titanium dioxide (N-doped TiO_2) for visible light photocatalysis," *New Journal of Chemistry*, vol. 40, no. 4, pp. 3000–3009, 2016.

[46] M. Dissanayake, J. Kumari, G. K. R. Senadeera, C. A. Thotawatthage, B. E. Mellander, and I. Albinsson, "A novel multilayered photoelectrode with nitrogen doped TiO_2 for efficiency enhancement in dye sensitized solar cells," *Journal of Photochemistry and Photobiology A: Chemistry*, vol. 349, pp. 63–72, 2017.

[47] S. P. Lim, A. Pandikumar, N. M. Huang, H. N. Lim, G. Gu, and T. L. Ma, "Promotional effect of silver nanoparticles on the performance of N-doped TiO_2 photoanode-based dye-sensitized solar cells," *RSC Advances*, vol. 4, no. 89, pp. 48236–48244, 2014.

[48] S. P. Lim, A. Pandikumar, H. N. Lim, R. Ramaraj, and N. M. Huang, "Boosting photovoltaic performance of dye-sensitized solar cells using silver nanoparticle-decorated N,S-co-doped-TiO_2 photoanode," *Scientific Reports*, vol. 5, no. 1, article 11922, 2015.

[49] J. Zhang, Q. Sun, J. Zheng et al., "The characterization of nitrogen doped TiO_2 photoanodes and its application in the dye sensitized solar cells," *Journal of Renewable and Sustainable Energy*, vol. 3, no. 3, article 033108, 2011.

[50] W. Guo, L. Wu, Z. Chen, G. Boschloo, A. Hagfeldt, and T. Ma, "Highly efficient dye-sensitized solar cells based on nitrogen-doped titania with excellent stability," *Journal of Photochemistry and Photobiology A: Chemistry*, vol. 219, no. 2-3, pp. 180–187, 2011.

[51] H. Tian, L. Hu, C. Zhang et al., "Retarded charge recombination in dye-sensitized nitrogen-doped TiO_2 solar cells," *The Journal of Physical Chemistry C*, vol. 114, no. 3, pp. 1627–1632, 2010.

[52] K. Prabakaran, S. Mohanty, and S. K. Nayak, "Improved electrochemical and photovoltaic performance of dye sensitized solar cells based on PEO/PVDF–HFP/silane modified TiO_2 electrolytes and MWCNT/Nafion® counter electrode," *RSC Advances*, vol. 5, no. 51, pp. 40491–40504, 2015.

[53] R. Gao, Y. Cui, X. Liu, and L. Wang, "Multifunctional interface modification of energy relay dye in quasi-solid dye-sensitized solar cells," *Scientific Reports*, vol. 4, no. 1, pp. 1–6, 2014.